SI Appendix for "Imaging local genetic influences on cortical folding": Supplemental Methods, Results and Figures

Alexander-Bloch et al., PNAS, 2020

Supplemental Methods

I. Image acquisition and processing

For the Genetics of Brain Structure and Function (GOBS) dataset (1,443 individuals), high resolution structural MRI was acquired on a Siemens 3T TIM Trio, using multiple T1-weighted 3D turbo-flash sequences with an adiabatic inversion contrast pulse (0.8-mm isotropic voxels, TE 3 ms, TR 2100 ms, TI 785 ms, flip angle 13°, FOV 200 mm). For the Human Connectome Project (HCP) dataset (1,113 individuals), structural scans were acquired on a Simens 3T Skyra. T1-weighted and T2-weighted structural images were acquired on a 3T Siemens Skyra employing a 32-channel head coil. T1 scans used a magnetization prepared rapid gradient echo sequence (0.7-mm isotropic voxels, TE 2.14 ms, TR 2240 ms, TI 1000 ms, flip angle 8°, ES 7.6 ms, GRAPPA 2). T2 scans used a variable flip angle turbo spin-echo sequence (0.7-mm isotropic voxels, TE 565 ms, TR 3200 ms, BW 744 Hz per pixel, no fat suppression pulse, GRAPPA 2).

FreeSurfer (version 5.3) was used for image processing as described previously (1, 2). Briefly, after normalization and skull stripping, white matter voxels were identified based on intensity and covered in a topologically corrected, tessellated mesh. This gray-white surface was then expanded to fit the pial surface. Surfaces were examined manually and edited if necessary. Cortical thickness was calculated as the distance between the gray-white surface and the pial surface at each vertex. Cortical curvature was used to register surfaces to an average surface containing 10,242 vertices per hemisphere (fsaverage5 surface). Mean curvature, a measure of cortical folding, was defined as the average of the principal curvatures at each vertex (3). By convention, the inward curvature of sulci is defined as positive, while the outward curvature of gyri is defined as negative.

For comparison, the Montreal Neurological Institute CIVET pipeline (version 1.1.10) was also used to calculate cortical thickness on the HCP sample, as previously described (4). Briefly, after registration and normalization, the inner and outer cortical surfaces for each hemisphere were constructed using a triangular mesh generated from a constrained Laplacian algorithm. Cortical thickness was calculated as the distance between the gray-white surface and the pial surface. For fidelity of comparison to FreeSurfer surfaces, the CIVET mesh containing 40,962 vertices was down-sampled to 9,895 uniform cortical regions by merging triangular faces into single regions (where the thickness of each region was the average of the thickness of the vertices within the region).

To increase the signal-to-noise ratio and the accuracy of registration to average templates, FreeSurfer surface data were smoothed with a 25-mm full-width at half-maximum (FWHM) smoothing kernel unless otherwise stated. Analyses were also performed with a 10-mm kernel to show robustness to this preprocessing step. CIVET data were smoothed using a 40-mm FWHM kernel, which is the default for the CIVET

www.pnas.org/cgi/doi/10.1073/pnas.1912064117

pipeline, so robustness to CIVET preprocessing also shows further robustness to the degree of smoothness.

Supplemental Methods II. Estimation of genetic correlations

Technical details of the variance decomposition and maximum likelihood estimation performed by SOLAR have been described previously (5). In the univariate case for a trait, *x*, across n subjects, the $n \times n$ covariance matrix (Ω) was modelled as

$$\Omega_{\mathrm{x}} = 2\Phi\sigma_{x_a}^2 + I_n\sigma_{x_e}^2, \quad (1)$$

where Φ is the kinship matrix of genetic relationships between subjects, $\sigma_{x_e}^2$ is the variance in *x* due to environmental effects, $\sigma_{x_a}^2$ is the variance in *x* due to additive genetic effects, and I is the identity matrix. After maximum likelihood estimation of these parameters, the heritability (h^2) of a trait is defined as $h^2 = \sigma_a^2/(\sigma_a^2 + \sigma_e^2)$.
In the bivariate case, for traits *x* and *y*, the $2n \times 2n$ covariance matrix can be partitioned as $\Omega_{\mathrm{z}} = \begin{pmatrix} \Omega_{\mathrm{x}} & \Omega_{\mathrm{xy}} \\ \Omega_{\mathrm{yx}} & \Omega_{\mathrm{y}} \end{pmatrix}$, where Ω_{x} and Ω_{y} are defined as per Equation (1), and the cross-covariance matrix is $\Omega_{\mathrm{xy}} = \Omega_{\mathrm{yx}} = 2\Phi\sigma_{xy_a}^2 + I\sigma_{xy_e}^2$. An alternative parametrization in terms of correlations rather than covariances is $\sigma_{xy}^2 = \sigma_x\sigma_y\rho$, where ρ is the correlation between *x* and *y*. Then Ω_{z} can be written as $\Omega_{\mathrm{z}} = 2\Phi \otimes \boldsymbol{A} + I_n \otimes \boldsymbol{E}$, where $\otimes$ is the Kronecker product, and the matrices ***A*** and ***E*** are the genetic and environmental components of
the variance, respectively:

$$\boldsymbol{A}=\begin{pmatrix} \sigma_{x_a}^2 & \sigma_{x_a}\sigma_{y_a}\rho_G \\ \sigma_{x_a}\sigma_{y_a}\rho_G & \sigma_{y_a}^2 \end{pmatrix} \text{ and } \boldsymbol{E}=\begin{pmatrix} \sigma_{x_e}^2 & \sigma_{x_e}\sigma_{y_e}\rho_E \\ \sigma_{x_e}\sigma_{y_e}\rho_E & \sigma_{y_e}^2 \end{pmatrix}.$$

Here, ρ_G is the correlation of the genetic components of the two traits, and ρ_E is the correlation of the environmental components of the two traits. The total phenotypic correlation, ρ, can be expressed in the terms estimated by the model as follows:

$$\rho = \sqrt{h_x^2 h_y^2}\rho_G + \sqrt{(1-h_x^2)(1-h_y^2)}\rho_E. \quad (2)$$

The correlation between an individual vertex and each of its neighbors was averaged to yield *L*ρ.

In the HCP data, the same variance-decomposition approach was used to calculate genetic correlations, leveraging the large number of twin pairs (243, 94 monozygotic) to generate the kinship matrix. However, reported phenotypic correlations were calculated directly by selecting one member of each family at random to generate a dataset of 457 unrelated individuals. In this case, the phenotypic correlation is estimated identically to “structural covariance” as described in numerous prior studies. We note that this more computationally efficient approach is not possible with the GOBS data because of the extended pedigree structure.

Supplemental Methods III. Estimation of orientation relative to sulcal-gyral axis

The sulcal-gyral axis (SGA) was calculated based on the difference in sulcal depth between each vertex, *v*, and *v*'s neighbors. Using a vertex randomly chosen from among the neighbors as the reference vertex, *r*, we calculated the angle between the arcs defined by *v-r* and *v-n* for all neighboring vertices, *n*. This calculation was based on the spherical law of cosines, which we operationalized using the normalized spherical projection of the FreeSurfer average cortical surface:

$$\cos c = \cos a \cos b + \sin a \sin b \cos C,$$

where *a*, *b*, and *c* are the arc lengths of the 3 sides of a spherical triangle on a unit sphere, and *C* is the angle opposite *c*. We then interpolated the expected change in sulcal depth at every angle from *0* to *360* degrees (relative to *v-r*), using a bilinear interpolation from the closest flanking vertices. SGA was defined as the axis of the smallest change in sulcal depth.

The same interpolation procedure was used to generate an estimate of the expected correlation at every angle (relative to SGA), and $O\rho$ was the difference between the correlations parallel to or close-to-parallel to SGA (average of 0_o +/- 30_o and 180_o +/- 30_o) and the correlations perpendicular to or close-to-perpendicular to SGA (average of 90_o +/- 30_o and 270_o +/- 30_o):

$$O\rho = (L\rho_{axial} - L\rho_{tan})/SD(L\rho),$$

where $SD(L\rho)$ is the standard deviation of all of the vertex's correlations (Supplemental Figure 11). Normalizing by the standard deviation of the vertex's correlations mitigates the effect of overall variability in the vertex's correlation (as opposed to the axial-transverse difference *per se*), but for comparison we also calculated orientation without this normalization step (Supplemental Figure 11). Note that both the axial and tangential directions are orthogonal to the radial direction, which points towards deeper white matter.

Note also that since $O\rho$ is expressed relative to SGA, it does not depend on the choice of the reference vertex, *r*, which is chosen from among *v*'s neighbors; however, to increase robustness to any numerical issues related to the interpolation of angles from *v-r*, we iteratively calculated $O\rho$ for every choice of *r* and took the median of these iterations as the reported estimate of $O\rho$. Code to calculate the orientation of local correlations is available at https://github.com/aaronab. Note that all estimates of orientation were based on phenotypic correlations.

Supplemental Methods IV. The spin test

See Supplemental Figure 3 for a schematic of the spin test.

An important methodological hurdle for this test is how to account for the medial wall (non-cortical areas in the FreeSurfer and CIVET surfaces). When maps are re-aligned at random, cortical areas become aligned with the medial wall. Our principal approach to this issue is to calculate the correspondence statistic (e.g. Pearson's

correlation coefficient, *r*) for the randomized alignments after excluding any vertices that were aligned with the medial wall. In general, the correspondence under random alignment (*r*R) was compared to the observed correspondence statistic (*rO*) to generate a *P* value. However, we also confirmed the results using an approach where *rR* was compared to *r'O* – the observed correspondence statistic after excluding any vertices that were aligned with the medial wall in the random alignment. In other words, *r'O* differs from *rO* in that it is re-calculated for each random alignment only using the vertices that were not excluded when calculating *rR*.

The statistical significance of local correspondence between two maps was quantified using a cluster-based version of the spin test. As described in the main text, local correspondence was defined at each vertex as the Pearson's correlation coefficient, *r*, between two maps including only vertices within a 10-mm geodesic distance of that vertex. Clusters of vertices (connected components on the mesh) were found that exceeded a nominal, moderate threshold for local correspondence (*r*>0.3 or *r*<–0.3). For each random alignment, the size of the largest such cluster (sum of the local correspondence at all vertices in the cluster, after *r-to-z* transformation) was used to generate a null distribution for comparison with the size of the clusters in the actual data. *P* values were empirically calculated for each cluster, *c*, as: (1 + number of random alignments in which largest cluster exceeded size of *c*)/(total number of random alignments tested). Note that this procedure provides control for multiple comparisons analogously to cluster-based Monte Carlo tests (6).

For these cluster-based comparisons, we weighted the size of the maximum cluster to account for the number of excluded vertices; that is, the size of the maximum cluster under each random alignment was:

$$S'_{maxclust} = S_{maxclust} \times \frac{V_{total}}{V_{total} - V_{exluded}}$$

where $S_{maxclust}$ is the size of the maximum cluster for that random alignment; V_{total} is the total number of cortical vertices under the anatomical (real) alignment; $V_{exluded}$ is the total number of cortical vertices excluded based on being aligned with medial wall vertices for that rotation; and $S'_{maxclust}$ is the weighted version of $S_{maxclust}$ used for the statistical comparison. Note that $S'_{maxclust} \geq S_{maxclust}$ for all random alignments, so this step increases the conservativeness of the cluster-based test.

In this manuscript we have adjusted the terminology used in our description of the spin test to emphasize that the test is not a permutation test in the usual sense. In the original manuscript (7), we used the terminology "spatial permutation test" while demonstrating that the test did not meet the ordinary assumptions of a permutation test, namely exchangeability at the vertex-level (i.e., spatial invariance of the vertex-vertex covariance structure under the null hypothesis). The theoretical basis for the test is in fact quite different from that of a classical permutation procedure. The "spin test" tests whether random alignment between the two maps could plausibly explain the degree of correspondence observed in the anatomical (real) alignment between the maps. In the formal sense, the test is conditioned on the two maps; it does not allow inference about dataset-to-dataset variability beyond the two maps. In an attempt to clarify this issue here, we use the terminology "randomization test of correspondence" rather than

"spatial permutation test of correspondence", although the algorithmic and theoretical basis of the test is identical to that described in the original publication.

Supplemental Methods V. Visualization

For visualization, we projected results onto the fsaverage5 inflated cortical surface as well as the flattened surface (8). On the flattened surface, the correlation of each vertex with each of its neighbors was visualized individually as an edge on the mesh. For consistency, the average CIVET surface was interpolated onto the fsaverage5 surface using nearest-neighbor interpolation, for purposes of visualizing CIVET results.

Supplemental Results

I. Relationship between phenotypic and genetic correlations

Although not previously demonstrated for brain morphology to our knowledge, the correspondence between phenotypic and genetic *L*ρ is predicted by prior studies in other disciplines. The argument that phenotypic correlations (ρ) can be used as a proxy for genetic correlations (ρ_G) has been called Cheverud's conjecture (9). Theoretically, both genetic and environmental causes of covariation are hypothesized to influence the growth and development of traits in the same direction and via the same pathways. Regardless of its theoretical basis, empirical support for the practical implementation of the conjecture is strong, with high correlations between ρ and ρ_G – and between ρ_G and the environmental correlation (ρ_E) – reported across pairs of morphological traits (10). Note that according to Supplemental Equation (2), a high correlation between ρ_G and ρ_E is mathematically unsurprising in the context of a high correlation between ρ_G and ρ across traits, assuming that all traits are moderately heritable as is cortical thickness in different cortical areas (h^2=0.3-0.5). (This statement is limited to the case of moderate heritability, because when $h^2 \rightarrow 1$ the phenotypic correlation is determined entirely by the genetic correlation and the influence of the environmental correlation is negligible.) For completeness, in our data we also assessed the relationship between genetic and environmental *L*ρ, and observed a significant correlation (r=0.29, P_{spin}=0.001, Supplemental Figure 2). We do caution against a strong biological interpretation of ρ_E, however, as the "environmental" component captures all of the variance not due to additive genetics in the statistical model (see Supplemental Methods II). In future investigations, it might be helpful to explicitly model specific aspects of the environment such as household effects.

Supplemental Results II. The effect of spatial proximity on local correlations

In all cases, downstream analyses of phenotypic or genetic correlations were performed as calculated after "regressing out" the global (non-linear) effect of distance on inter-regional correlations, whereby vertices that are closer together are also expected to be more strongly correlated. Without this regression step, the smoothing of the vertices (which is necessary for inter-subject registration) will artificially inflate measures of correlation. Moreover, the distance between neighboring vertices on the cortical mesh is not uniform on the cortical surface – and in fact has a non-trivial relationship with cortical curvature – which could be an artifactual cause of spatial variation in the average correlation between a vertex and its neighbors (Supplemental Figure 13A). This variability in the distance between neighboring distances is addressed by using the residuals after controlling for the relationship with distance (Supplemental Figure 13B). Note that more highly smoothed data is less biased by a distance effect. Also note that regressing out distance is expected to remove only spatially invariant ("global") effects of distance as the statistical model includes all neighboring vertices across the cortex. In other words, the signal of interest, which pertains to spatial variability in local correlations, is not removed by the regression step. The effect of distance was

calculated separately for phenotypic and genetic correlations, as well as for each of the alternative methods for determining a vertex's local neighborhood. It is worth pointing out that sulcal fundi tend to have shorter distances to their neighbors on average, but we find that they tend to have lower average correlations – the opposite effect of what would be expected if the effect were due to a distance confound.

As a supplement to this approach of dealing with the potential confounds of anatomical distance and smoothing, we also implemented a "center-ring" alternative to smoothing. Starting with non-smoothed data, for each vertex we calculated *i*) the mean thickness of all vertices within a 5-mm geodesic distance (the "center"), and *ii*) the mean thickness of all vertices in between a 5-mm and 7-mm distance (the "ring"). Across individuals, we estimated the correlation between the thickness in the center and the thickness in the ring to obtain an alternative measure of $L\rho$. Note that with this approach, the distance between the traits does not vary across vertices. This approach also decreases the spatial scale of smoothing relative to the spatial scale of interest, and minimizes the likelihood that results are dependent on spatial blurring across neighboring vertices. Importantly, the main result of association with mean curvature is replicated using this approach (r=–0.30, P_{spin}=0.001, Supplemental Figure 7).

Supplemental Results III. Consistency across methodological choices

As described in the main text, the baseline pattern of local correlations was tested for robustness against multiple methodological perturbations (see Supplemental Figure 4). Unless stated otherwise, results in the main text are reported for phenotypic $L\rho$ calculated with the HCP data, a 25-mm FWHM smoothing kernel, FreeSurfer processing and a 10-mm geodesic distance on the cortical mesh as the local neighborhood. (Note that this geodesic distance was calculated on the mid-gray cortical surface, equidistant between pial surface and the cortical white matter.) In the HCP dataset, phenotypic $L\rho$ was easily calculated from a subset of unrelated individuals (in contrast to the extended pedigree structure of GOBS, which is optimized for genetic analyses). Compared to decomposing phenotypic correlations into genetic and environmental components, this step reduces computation time by a factor greater than 100; without this step, the set of analyses conducted in this paper would be computationally intractable. The simplifying assumption to focus on phenotypic correlations (also known as "structural covariance") is justified by prior precedent in the literature (see Supplemental Results I) and by the observed correspondence between phenotypic and genetic $L\rho$ in our data (see Main Figure 1).

The choice to focus on the 10-mm geodesic neighborhood for the comparisons with cortical folding was motivated in particular by the larger amount of data available for the interpolation step in the calculation of the orientation of local correlations ($O\rho$), which is expected to increase signal-to-noise. Indeed, the pattern of $O\rho$ appeared much less noisy when vertices within a 10-mm geodesic were considered neighbors (Supplemental Figure 9) as opposed to when only the 6 adjacent vertices on the cortical mesh were considered neighbors (Supplemental Figure 12). The correspondence between maps of $O\rho$ calculated using these different definitions of the local neighborhoods was small in magnitude though statistically significant (r=0.08,

P_{spin}<0.001). In contrast, the correspondence between maps of $L\rho$ using these different definitions of neighborhood was higher (r=0.68, P_{spin}<0.001), which likely reflects the fact that in this calculation the correlations (between a vertex and its 6 adjacent neighbors) were averaged rather than used as a basis for interpolation.

As an additional control, we replaced total brain volume with mean total cortical thickness as a covariate in the calculation of inter-vertex correlation and $L\rho$. The correspondence with maps calculated using total brain volume as a regressor was high (r=0.87, P_{spin}<0.001), and the correspondence with folding was preserved (r=–0.29, P_{spin}<0.001), implying that the pattern of $L\rho$ was not driven by global inter-individual differences in cortical thickness.

Supplemental Results IV. Childhood Sample

An important issue for the set of analyses is the appropriateness of developmental inferences based on adult neuroimaging samples. To complement the adult samples (GOBS and HCP) we performed an analysis using the Philadelphia Neurodevelopmental Cohort (PNC), specifically using 8-9-year-olds available in the study (n=98, with 32 scanned at age 8 and 66 scanned at age 9; 48 female and 50 male subjects). Briefly and as described previously (11), data were acquired using a single Siemens Tim Trio (Erlangen, Germany) 3T scanner using a 3D inversion-recovery, magnetization-prepared rapid acquisition gradient echo (MPRAGE) sequence (TI/TR/TE 1100/1810/3.51 ms, flip angle 9°, matrix 256×192, FOV 240×180mm, voxel resolution 0.93×0.93×1.0 mm_3 . FreeSurfer (version 5.3) was used to generate maps of cortical thickness as described above. For this supplemental analysis, we focused on 25-mm FWHM smoothed data using the 10-mm geodesic neighborhood for the calculation of phenotypic $L\rho$.

The childhood data corroborated the principal findings in the adult datasets. We observed a strong correlation between the $L\rho$ *PNC* and the $L\rho$ *HCP* using the same methodological procedures *(r=0.67, P_{spin}<0.001).* Further, there was significant correspondence between $L\rho$ PNC and folding as measured by mean curvature *(r=–0.32, P_{spin}<0.001)*. See Supplemental Figure 5.

Supplemental Results V. Heritability of curvature

It is important to clarify the distinction between our main analyses and an analysis of the heritability of thickness or curvature *per se*. Although genetic correlations are not interpretable for traits that are not heritable, the degree of correlation is independent of the magnitude of heritability. Genetic $L\rho$ is a measure of the overlap between genetic factors that influence thickness in neighboring vertices, which can be high even if most of the inter-individual variance in thickness is due to non-genetic factors. Moreover, and consistent with prior studies (12), supplemental analysis in the GOBS dataset shows a heterogenous map of vertex-level heritability of curvature, which is markedly lower overall than the heritability of thickness. The map of curvature heritability does not correspond spatially to the map of mean curvature (r=–0.01, P_{spin}=0.73, Supplemental

Figure 10), meaning that there is no consistent difference in the heritability of curvature in gyri versus sulci. The heritability of curvature does appear to be higher in the vicinity of primary sulci including primary motor cortex which is broadly consistent with our results. However, the lack of a straightforward correlation between mean curvature and the heritability of curvature implies that spatial gradients in $L\rho$ track a different phenomenon than the heritability of curvature. Curvature may also be a noisier measurement than thickness, limiting the interpretability of the magnitude of heritability at the vertex level. Importantly though, our results do not imply that folding is under genetic control only in a subset of sulci. Rather, while folding appears to be related to local thickness co-variance in a subset of sulci, it is expected that other genetic factors influence inter-individual variation in curvature in a regionally heterogenous fashion. A full account of these other factors is beyond the scope of the present study.

Supplemental Results VI. Does thickness drive local thickness co-variance?

Given that gyral crowns tend to be thicker than sulcal fundi, and that we find that $L\rho$ tends to be lowest in sulcal fundi, it is possible that differences in thickness itself drive the observed difference in genetic $L\rho$. Such a correspondence could be due to non-biological factors differentially increasing noise in thinner areas of cortex, which could in turn decrease inter-vertex correlation. To test this notion, we undertook a supplemental analysis to directly assess the correspondence between thickness and phenotypic $L\rho$. The correspondence between these maps is low and not statistically significant (r=0.02, P_{spin}=0.91), which makes it unlikely that gross differences in thickness drive the observed spatial variability in $L\rho$.

References

1. A. M. Dale, B. Fischl, M. I. Sereno, Cortical surface-based analysis. I. Segmentation and surface reconstruction. *Neuroimage* **9**, 179–194 (1999).
2. B. Fischl, *et al.*, Automatically parcellating the human cerebral cortex. *Cereb. Cortex* **14**, 11–22 (2004).
3. R. Pienaar, A methodology for analyzing curvature in the developing brain from preterm to adult. *Int. J. Imaging Syst. Technol.* **18**, 42–68 (2008).
4. J. S. Kim, *et al.*, Automated 3-D extraction and evaluation of the inner and outer cortical surfaces using a Laplacian map and partial volume effect classification. *Neuroimage* **27**, 210–221 (2005).
5. J. T. Williams, P. Van Eerdewegh, L. Almasy, J. Blangero, Joint multipoint linkage analysis of multivariate qualitative and quantitative traits. I. Likelihood formulation and simulation results. *Am. J. Hum. Genet.* **65**, 1134–1147 (1999).
6. T. E. Nichols, A. P. Holmes, Nonparametric permutation tests for functional neuroimaging: a primer with examples. *Hum. Brain Mapp.* **15**, 1–25 (2002).
7. A. F. Alexander-Bloch, *et al.*, On testing for spatial correspondence between maps of human brain structure and function. *Neuroimage* (2018).
8. B. Fischl, M. I. Sereno, A. M. Dale, Cortical surface-based analysis. II: Inflation, flattening, and a surface-based coordinate system. *Neuroimage* **9**, 195–207 (1999).
9. J. M. Cheverud, A comparison of genetic and phenotypic correlations. *Evolution (N. Y).* **42**, 958–968 (1988).
10. S. M. Sodini, K. E. Kemper, N. R. Wray, M. Trzaskowski, Comparison of genotypic and phenotypic correlations: Cheverud's conjecture in humans. *Genetics* (2018).
11. T. D. Satterthwaite, *et al.*, Neuroimaging of the Philadelphia neurodevelopmental cohort. *Neuroimage* **86**, 544–553 (2014).
12. T. Ge, *et al.*, Massively expedited genome-wide heritability analysis (MEGHA). *Proc. Natl. Acad. Sci. U. S. A.* **112**, 2479–2484 (2015).

Supplemental Figures

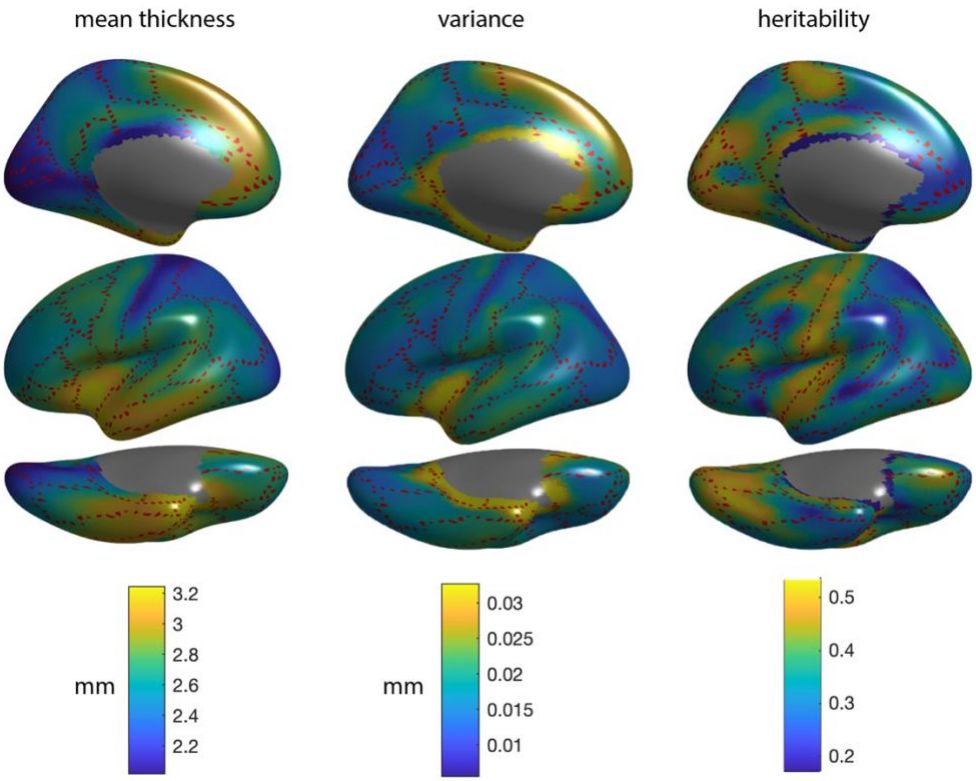

Supplemental Figure 1. Genetic influence on cortical thickness. From left to right, mean cortical thickness, variance of cortical thickness and heritability of cortical thickness. Calculated on GOBS data with FreeSurfer using 25-mm full-width at half-maximum (FWHM) smoothing kernel. The dashed red lines mark boundaries between the gyral regions in Freeserfer's Desikan atlas, such that that the dashed lines generally occur within sulcal fundi.

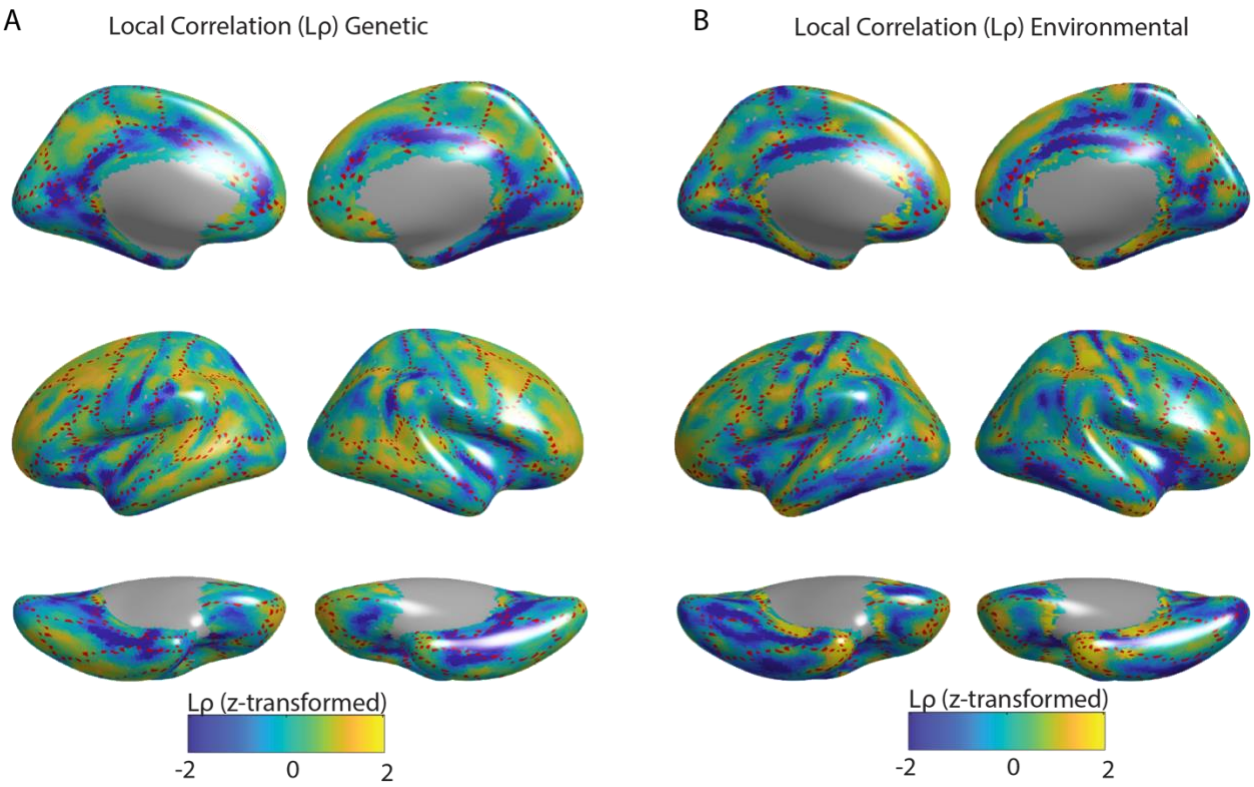

Supplemental Figure 2: Correlated genetic and environmental local influences on cortical thickness. Analogous to Main Figure 2 but showing **A**) the genetic component of the average local correlation (*Lρ*) compared to **B**) the environmental component of the *Lρ*.

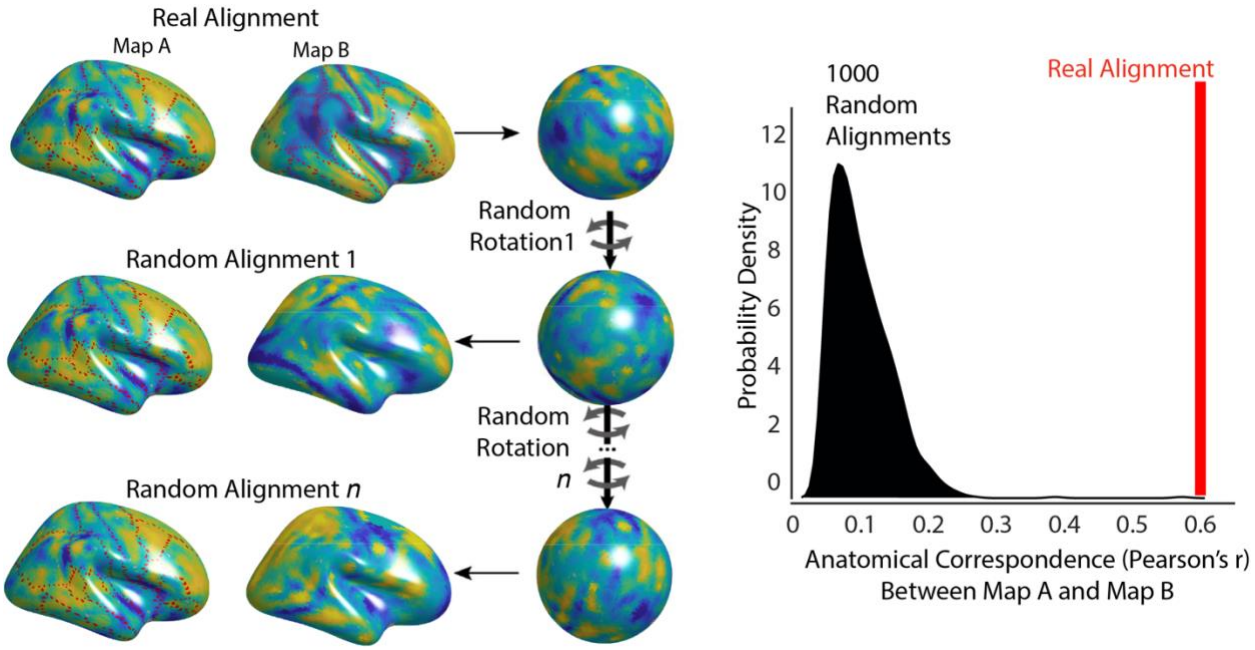

Supplemental Figure 3. Schematic of spin test. To test the significance of the anatomical correspondence between maps, we generate an empirical null distribution for the correspondence statistic (Pearson's correlation coefficient, *r*) using an alignment randomization based on random rotations of a spherical projection of the cortical surface (the "spin test"), where the correlation was recalculated after the maps were rotated relative to one another. The *P* value was calculated based on the number of times the correlation from the randomly-aligned data equaled or exceeded the correlation the data in their observed alignment. Here, the two maps are phenotypic and genetic $L\rho$ (r=0.6, P_{spin} <0.001).

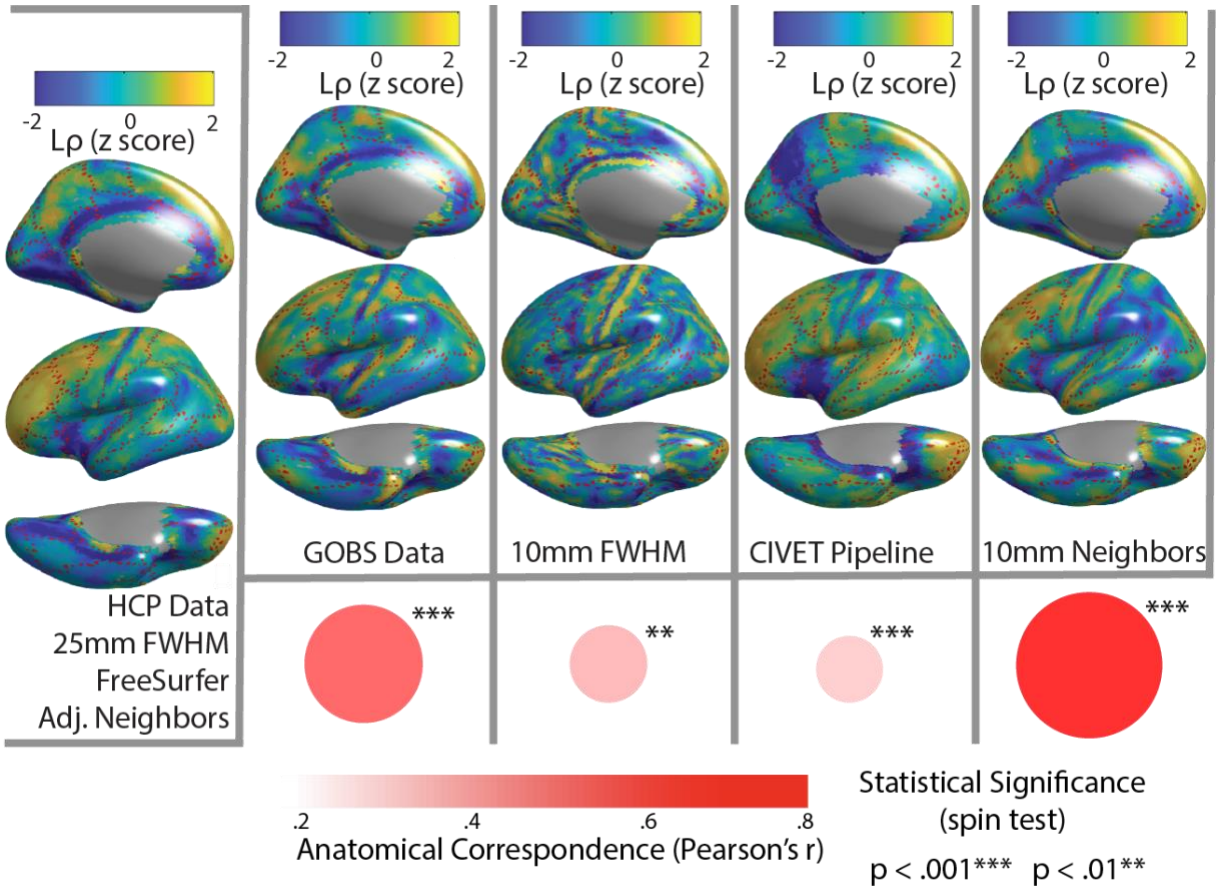

Supplemental Figure 4: Robustness to methodological perturbation, for the estimation of phenotypic local correlation (*Lρ*). The map to the far left was generated using data from the Human Connectome Project (HCP); processed using FreeSurfer with a 10-mm full-width at half-maximum (FWHM); and with each vertex's local neighborhood defined as the set of (in general six) adjacent vertices on the cortical mesh. From left to right, one aspect of the methodological pipeline was perturbed and the map of phenotypic local correlation (*Lρ*) was re-estimated: using data from the Genetics of Brain Structure and Function Study (GOBS); using a 10-mm FWHM smoothing kernel; using the CIVET preprocessing pipeline; defining each vertex's local neighborhood (from which the mean local correlation is averaged) within 1 cm (geodesic distance). In the panel, both the redness and the size of the circles is proportional to the correspondence between the maps (Pearson's *r*) and the statistical significance is calculated based on the spin test illustrated in Supplemental Figure 3.

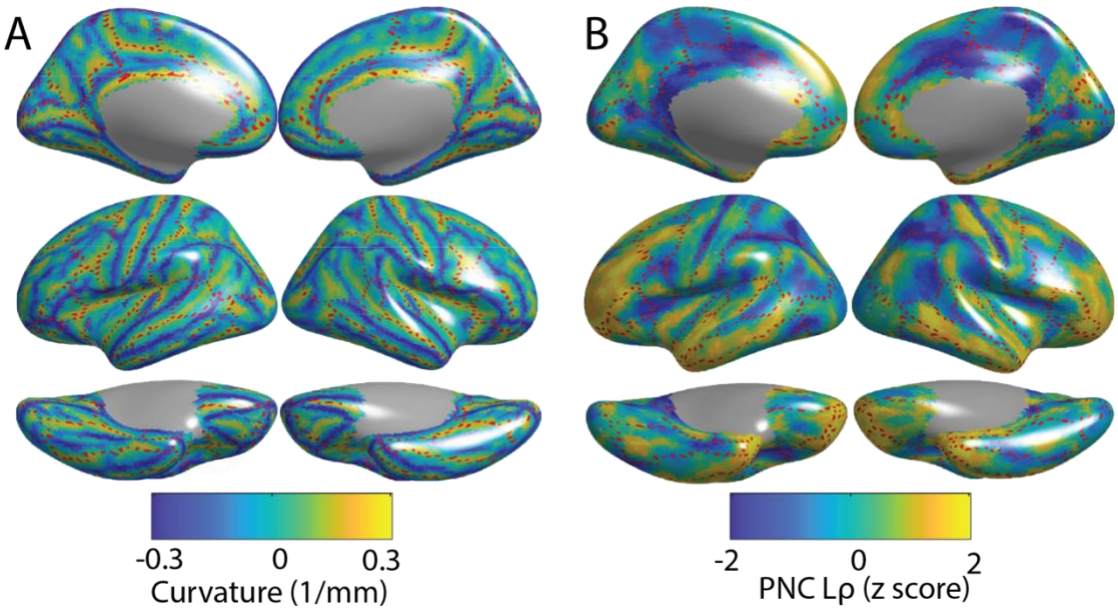

Supplemental Figure 5: Replication in a childhood sample of 98 children aged 8-9 from the Philadelphia Neurodevelopmental Cohort (PNC). Here we show the organization of mean phenotypic local correlation (*Lρ*) and its relationship with gyral-sulcal organization as measured by mean curvature, analogous to Main Figure 4 but using a childhood sample. **A**) Map of mean curvature. Sulci are positively curved, while gyri are negatively curved. **B**) Map of *Lρ*.

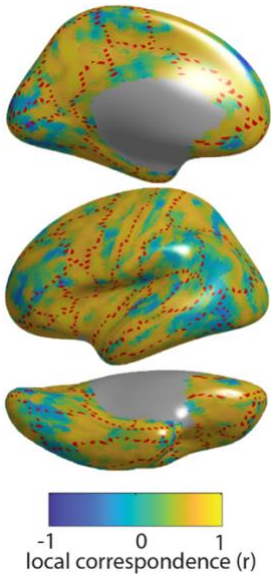

Supplemental Figure 6: The left-right symmetry of local correlations in cortical thickness (*Lρ*). Map of local correspondence between left hemisphere *Lρ* and right hemisphere *Lρ*, visualized on the left hemisphere surface.

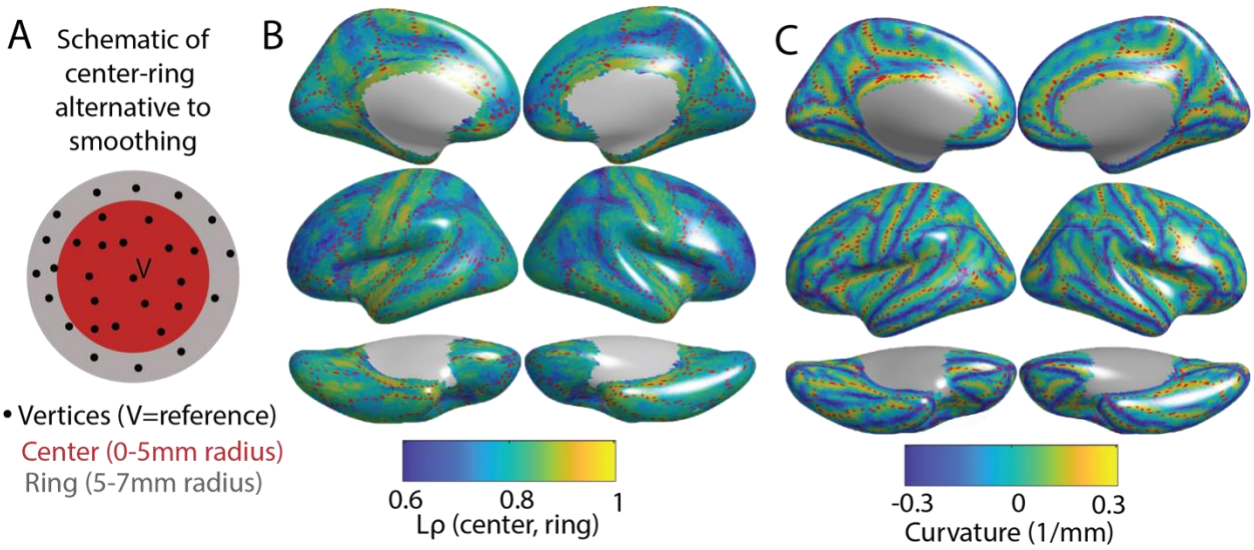

Supplemental Figure 7: Alternative center-ring approach to calculating phenotypic local correlation (*Lρ*) and its relationship with gyral-sulcal organization as measured by mean curvature. **A**) Schematic of center-ring approach. For each vertex, *V*, the thickness of all vertices within a 0- to 5-mm radius are averaged to yield *V*'s center; the thickness of all vertices within a 5- to 7-mm radius were averaged to yield *V*'s ring. **B**) Map of *Lρ*, calculated as Pearson's correlation, *r*, between V_{center} and V_{ring} across individuals for all *V*. **C**) Map of mean curvature. Sulci are positively curved, whereas gyri are negatively curved.

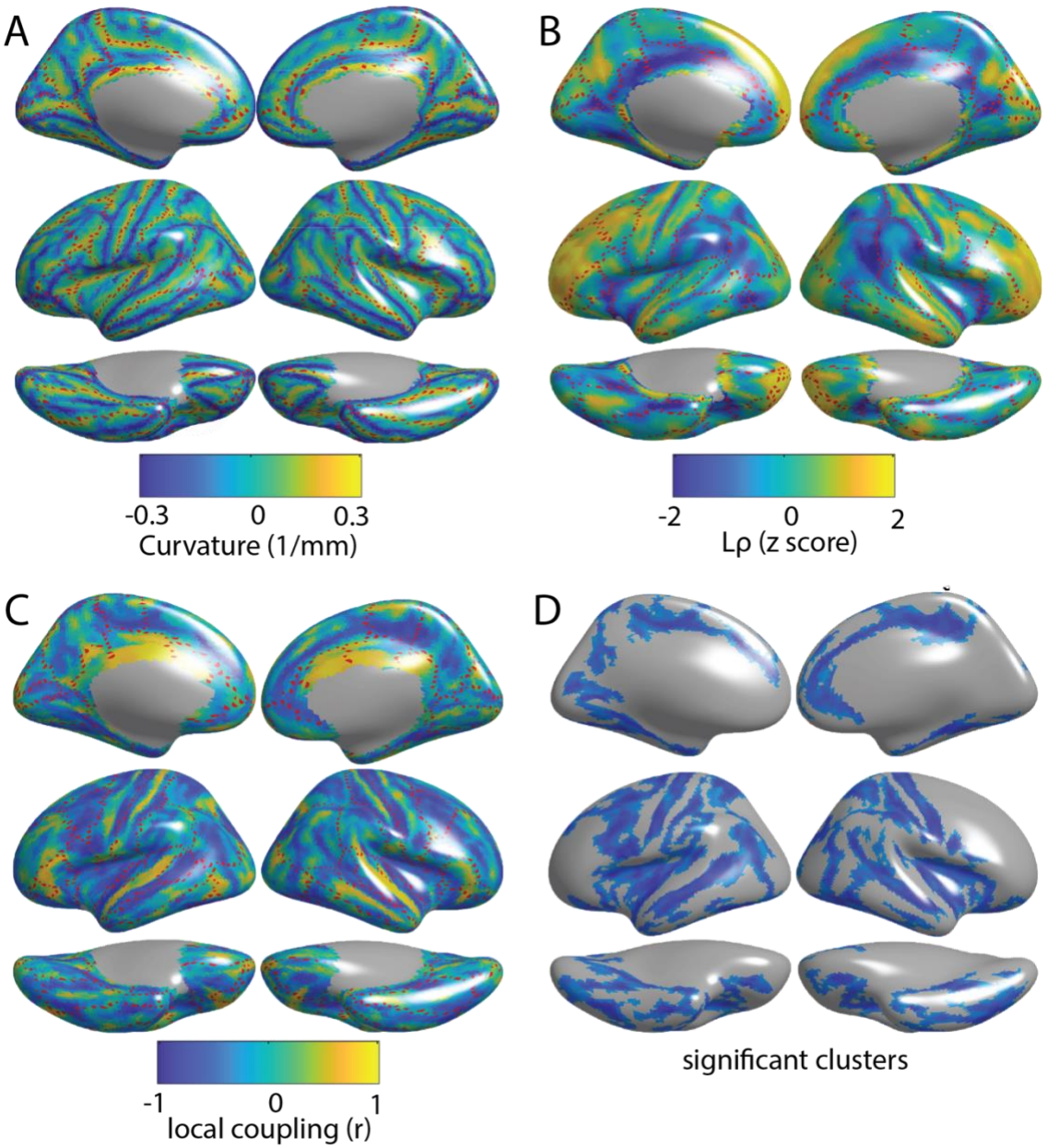

Supplemental Figure 8: Mean phenotypic local correlation (*Lρ*) and its relationship with gyral-sulcal organization as measured by mean curvature, analogous to Main Figure 4 but showing both cerebral hemisphers. **A)** Map of mean curvature. Sulci are positively curved, while gyri are negatively curved. **B)** Map of *Lρ*. **C)** Map of local correspondence between mean curvature and *Lρ*. **D)** Significant clusters of local correspondence based on the spin test.

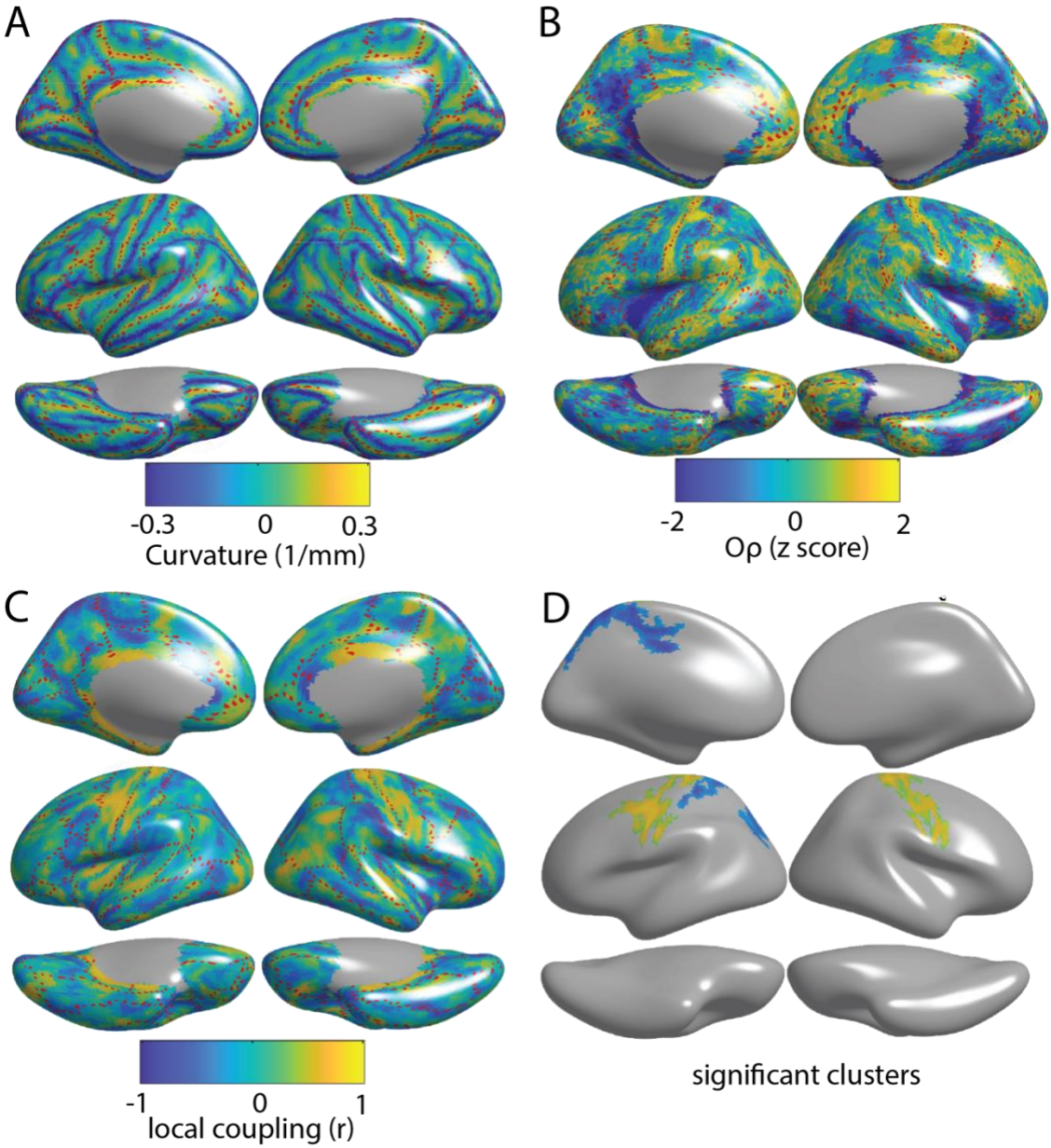

Supplemental Figure 9. Orientation of local correlations (*Oρ*) and its relationship with gyral-sulcal organization as measured by mean curvatures. **A)** Map of mean curvature. Sulci are positively curved, while gyri are negatively curved. **B)** Map of *Oρ*. **C)** Map of local correspondence between mean curvature and *Oρ*. **D)** Significant clusters of local correspondence based on the spin test.

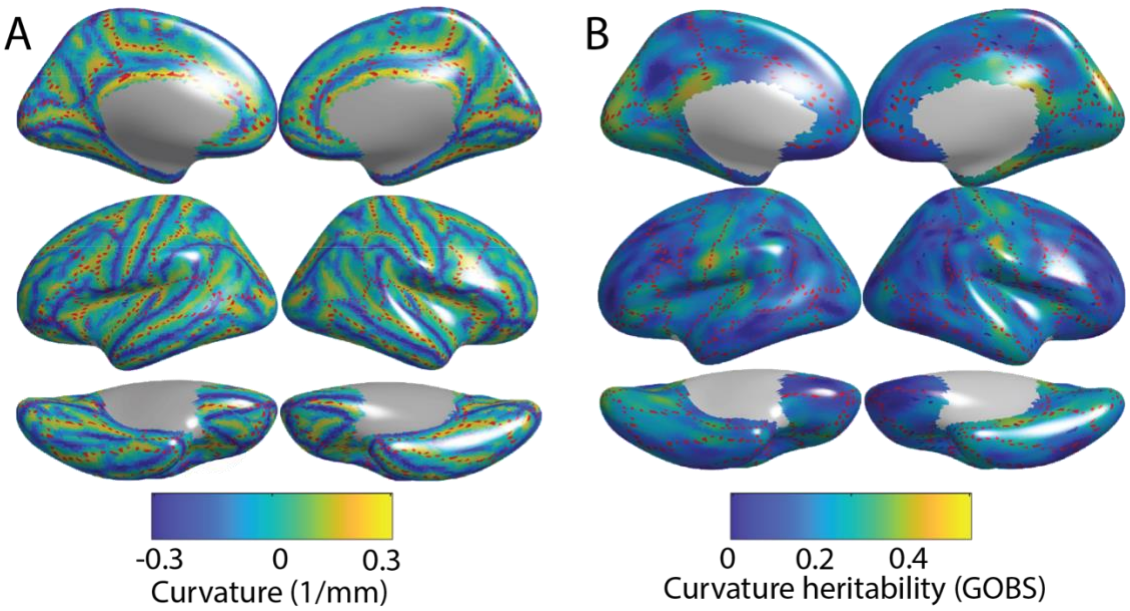

Supplemental Figure 10: The relationship between the population average of mean curvature and the heritability of mean curvature across vertices. **A**) Map of mean curvature. Sulci are positively curved, while gyri are negatively curved. **B**) Map of the heritability of mean curvature.

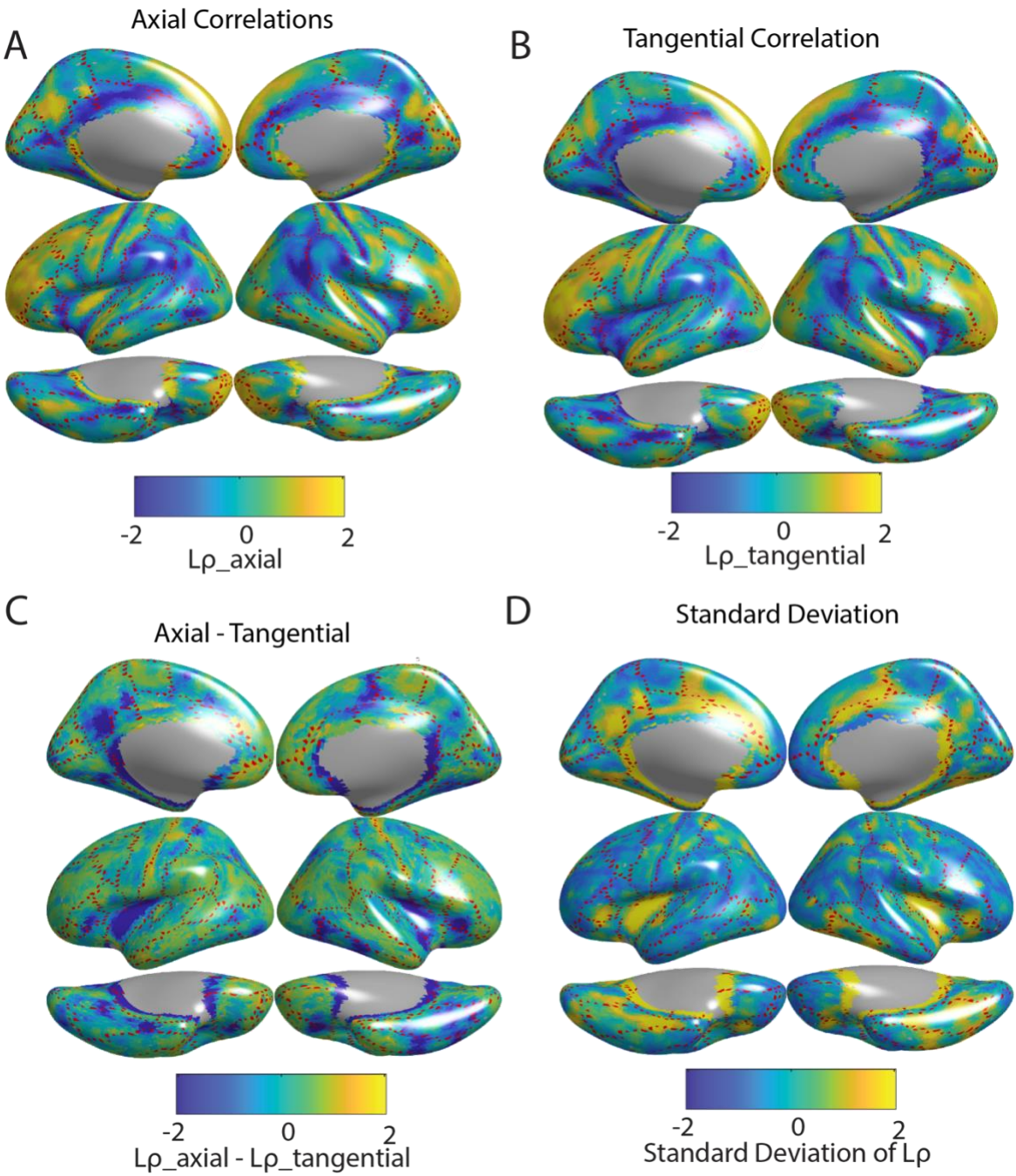

Supplemental Figure 11: The component maps used in the calculation of the orientation of local correlations. Distinct maps for the axial **(A)** and tangential **(B)** components of local correlation (see Supplemental Methods III). *Oρ* is defined as the axial component minus the tangential component **(C)**, divided by the standard deviation of the local correlation at each vertex **(D)**. Supplemental Figure 9 shows the map of *Oρ* and its relationship with folding.

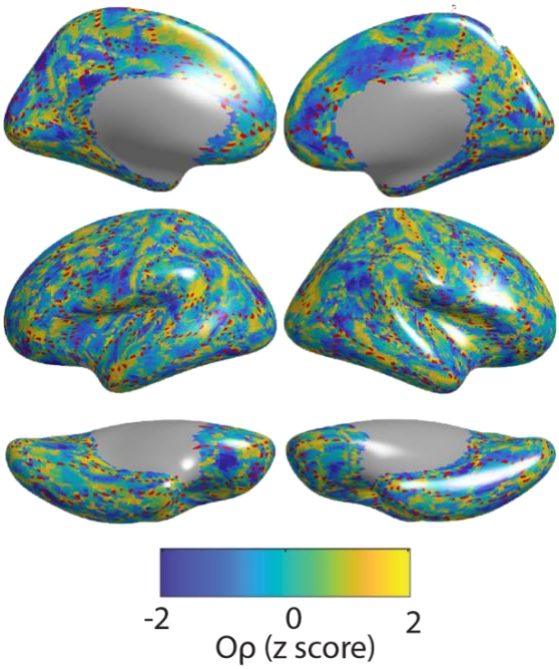

Supplemental Figure 12: Orientation of local correlations (*Oρ*) with an alternative definition of a vertex's local neighborhood. Here, neighborhood was defined as adjacent vertices on the cortical mesh, as opposed to all vertices within a 1cm geodesic distance, as in Supplemental Figure 9.

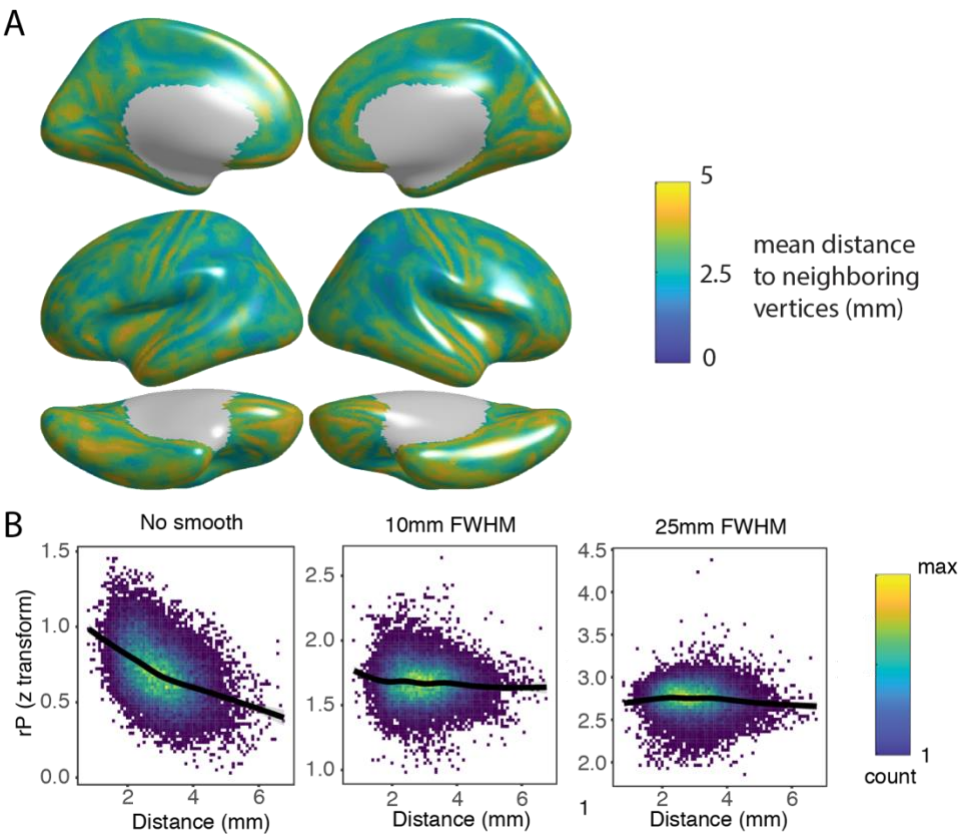

Supplemental Figure 13: Distance effects on local correlation measures. **A)** The map of average distance between a vertex and its direct neighbors on the cortical mesh. B) Plots of the relationship between phenotypic correlation and distance across pairs of neighboring vertices.